International Journal of Heat and Fluid Flow 114 (2025) 109779

Contents lists available at ScienceDirect

International Journal of Heat and Fluid Flow

journal homepage: www.elsevier.com/locate/ijhff

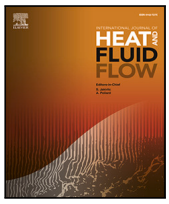

Compressed representation of separation bubbles from a vast database

Virginia Bologna *, Matteo Dellacasagrande, Davide Lengani, Daniele Simoni

University of Genova, MASET, DIME, Via Montallegro, 1, Genova, 16145, Italy

ARTICLE INFO

Keywords:
Laminar Separation Bubble (LSB)
Proper Orthogonal Decomposition (POD)
Data reduction
High Performance Computing (HPC)

ABSTRACT

The present work describes a wide experimental database of laminar separation bubbles formed on a flat plate for different Reynolds numbers, adverse pressure gradients and free-stream turbulence intensity levels. The database accounts for 72 different combinations of the aforementioned parameters, for which both short and long bubble types have been observed. For each flow case, a set of 6000 snapshots has been acquired using a fast response Particle Image Velocimetry system. In this work all the 72 × 6000 images have been used simultaneously to construct a large snapshot matrix containing both the statistical and the dynamic response of the bubble to the flow parameters variation. To handle such a large snapshot matrix, a parallelized version of the Proper Orthogonal Decomposition routine is presented to be adopted in High-Performance Computing environment. The reduction of the high dimensional database into a low-order model retaining few POD modes and coefficients has been obtained. Particularly, two subsets of modes capturing the time-averaged and dynamic response of the bubble have been detected based on the frequency spectra of the related coefficients. It will be shown that dimensionality can be reduced up to about 1%, while retaining the generalized response of a laminar separation bubble. The present work therefore shows the existence of a reduced state space over which the response of a LSB evolves for a wide range of the leading influencing parameters.

1. Introduction

Boundary layer (BL) separation may occur in case of strong adverse pressure gradients (APG), low Reynolds numbers and low free-stream turbulence intensity ($FSTI$) levels, e.g., Tani (1964). If the boundary layer transitions to turbulence and then reattaches to the wall, a laminar separation bubble (LSB) forms on the solid surface, e.g., Horton (1968). Due to the high turbulence production in separated boundary layers, the occurrence of a LSB is detrimental for the aerodynamic performances of wings, turbomachinery blades and other industrial components, e.g., Tucker (2013). As the shear layer detaches from the wall, it becomes inviscidly unstable, e.g., Diwan and Ramesh (2009), Brinkerhoff and Yaras (2011). Disturbances are amplified via the Kelvin–Helmholtz type instability, which leads to the formation of 2D spanwise rolls near the maximum displacement of the bubble, e.g., Hosseinverdi and Fasel (2019), Marxen et al. (2013). Their successive three-dimensional breakdown then leads to the turbulent reattachment of the boundary layer, e.g., Marxen et al. (2013), Kurelek et al. (2021). This phenomenon has been extensively studied in the last decades by means of experiments (Marxen et al., 2003, Radespiel et al., 2007) and numerical simulations (Avdis et al., 2009, Alferez et al., 2013 Sandham, 2008, Hosseinverdi and Fasel, 2019 Rodríguez et al., 2021, Alam and Sandham, 2000 Marxen et al., 2004). Since changes in the inlet flow characteristics can have significant impact on the time-mean and dynamical properties of a LSB, many efforts have been spent in the past in the understanding of the bubble response to changes in the external flow parameters, see e.g., Eljack et al. (2021), Kumar and Sarkar (2023), Sengupta et al. (2019) to name a few.

The time-mean and dynamic behavior of a laminar separation bubble are mostly affected by changes in the Reynolds number, turbulence intensity and streamwise pressure gradient, e.g., McAuliffe and Yaras (2010), Avdis et al. (2009), Boutilier and Yarusevych (2012), Istvan and Yarusevych (2018), Dellacasagrande et al. (2020). Among these parameters, the flow Reynolds number plays the major role in the definition of the bubble size and dynamics. The higher the Reynolds number the lower the size of a LSB (Roberts, 1975) and the higher the dominant shedding frequency (Boutilier and Yarusevych, 2012). This latter scales in inverse proportion to the boundary layer thickness at the separation position (Simoni et al., 2017), which reduces at higher Reynolds numbers. Under low $FSTI$ and elevated APG, reducing the Reynolds number may result in the sudden and marked increase of the bubble height and length, with the laminar separation bubble possibly switching from a short to a long configuration. This phenomenon is termed in the literature as the bursting process (Gaster, 1967, Mitra and Ramesh, 2019), which causes strong modification of the surface pressure distribution as well as marked drop in performances (Sandham,

* Corresponding author.
E-mail address: virginia.bologna@edu.unige.it (V. Bologna).

https://doi.org/10.1016/j.ijheatfluidflow.2025.109779
Received 17 May 2024; Received in revised form 30 September 2024; Accepted 12 February 2025
Available online 28 February 2025
0142-727X/© 2025 The Authors. Published by Elsevier Inc. This is an open access article under the CC BY license (http://creativecommons.org/licenses/by/4.0/).

2008, Jaroslawski et al., 2023). The response of a LSB to Reynolds number variation and the onset of the bursting process have been studied both experimentally and via numerical simulations by Horton (1967), Diwan et al. (2006), Alferez et al. (2013) and Serna and Lázaro (2015) to name a few. Among others, Toppings and Yarusevych (2023) have provided an exhaustive study of changes in the time-average and dynamic behavior of a LSB when varying the Reynolds number at fixed $FSTI$. The effects of time-varying flow velocity on the formation and bursting of a LSB have been shown. During formation and bursting transients, the changes in the unstable frequencies of the separated shear layer have seen to show similar Reynolds number dependency to quasi-steady flows, see also Toppings and Yarusevych (2024).

The analogous response of a LSB to Reynolds number reduction is observed when lowering the free-stream turbulence. The cause for bubble enlargement, and bursting, is in this case the lowering of free-stream forcing rather than the modification of the inherent stability characteristics of the separated shear layer, e.g., Marxen et al. (2004), Marxen and Henningson (2011). As bursting occurs due to Reynolds number and $FSTI$ reduction, the onset of absolute instability can be observed in place of the convective instability mechanism driving transition in short like bubbles, see e.g., Wu et al. (2020) and Jones et al. (2008). The change in the bubble size, state (i.e. short and long one) and dynamics has been documented also as a consequence of the modification of pressure gradient and angle of attack. Eljack et al. (2021) have observed the occurrence of short and long laminar separation bubbles on an airfoil depending on the angle of attack and Reynolds number. For both bubble states, the frequency content of disturbances developing in the separated shear layer has been found to move from higher to lower frequencies when increasing the streamwise pressure gradient. Aniffa et al. (2023) have compared the statistical and dynamic properties of pressure- and geometry-induced LSBs for different free-stream turbulence intensity levels and Reynolds numbers. The vortex shedding frequency of a separated shear layer has been shown to remain unchanged for the geometry-induced cases even with an enhanced level of free-stream turbulence. Contrarily, it has been found to vary for the pressure-induced case. For pressure-induced LSBs, Klebanoff modes have been also observed to form in the separated shear layer and to distort the 2D spanwise rolls still forming due to K-H type instability. Depending on the combination of the flow parameters, different structures are therefore expected to coexist within a LSB, e.g., Istvan and Yarusevych (2018) and Verdoya et al. (2021).

The above mentioned works reveal the complexity of separated flows as well as the difficulty in capturing the general response of a LSB to the variation of the flow parameters. Indeed, different flow structures (e.g., streaks and spanwise rolls) can coexist within a LSB, which may undergo different types of instability mechanisms (e.g., convective or absolute ones) leading to different bubble states (short and long ones). Changes in the Reynolds number, $FSTI$ and APG therefore affect not only the time-mean bubble shape, but also its stability characteristics and dynamics. In this sense, the current literature works, of which few examples have been reported above, provide an exhaustive view of the response of a LSB to the variation of a single or multiple flow parameters in terms of statistical and dynamic properties of the separated shear layer. Nevertheless, to the best of authors' knowledge, the existence of a reduced state-space capturing a common and general response of a LSB for a wide variation of the influencing parameters has not yet been investigated. This might answer the question if different separated flows evolving under largely different flow condition, still share similarities in terms of statistics and dynamic content. In the previous authors' work (Dellacasagrande et al., 2023), a data driven approach based on Proper Orthogonal Decomposition (POD) has been used to highlight the existence of a low dimensional space capturing the time-averaged response of short and long LSBs to Reynolds number, free-stream turbulence intensity and pressure gradient variation. This work extends the previous investigation including also the analysis of the dynamic behavior of the separated shear layer, in terms of frequency content, and how it is affected by the flow parameters variation. To this end, 72 different combinations of Reynolds number, APG and $FSTI$ have been considered for the generation of LSBs of different dimensions, frequency contents and states. All flow cases have been processed simultaneously to extract a unique data driven state space capturing the overall response of the separation bubble. Since POD is suitable for construction of reduced order representation of complex systems (Fogleman et al., 2004, Voisine et al., 2011, Vitkovicova et al., 2020), a parallelized version of the POD routine in an high performing computing (HPC, (Bi and Ono, 2013; Sayadi and Schmid, 2016)) environment is proposed to handle the large amount of data here collected. The parallelized POD procedure adopted is detailed in the present study. POD will be shown to extract modes and mixed temporal-flow-case coefficients describing the general response of the bubble to the variations of the main influencing parameters.

Table 1
Turbulence-generating grids characteristics: free-stream turbulence intensity ($FSTI$), bars width (d), mesh size (M), and porosity parameter $P = (1 - \frac{d}{M})^2$.

Case	$FSTI$ [%]	d [mm]	M [mm]	P
No-Grid	1.5	–	–	–
Low-Tu	2.5	2	8	0.64
High-Tu	3.5	4	8	0.36

2. Experimental setup and measuring techniques

LSBs embodied in the present database have been acquired in the low-speed open-loop wind tunnel installed in the Aerodynamic and Turbomachinery Laboratory of the University of Genova. Measurements have been performed over a thick flat plate, with an elliptic leading edge (4:1), in order to avoid uncontrolled flow separation at the junction that may alter the transition process on the rear part of the plate. The plate is 300 mm long and 300 mm wide, producing 2D time-average flow in the meridional section of the plate (Verdoya et al., 2021). In order to minimize trailing edge effects that may influence the evolution of LSBs (Nakamura et al., 1991), a 100 mm long wedge shaped trailing edge extension has been employed.

The front part of the test section, from the plate leading edge to the geometrical throat of the channel, has a converging fixed geometry which accelerates the flat plate boundary layer. Instead, in the rear part of the channel, the plate is inserted between two adjustable end-walls, which allow changing the pressure distribution applied to the boundary layer (see Fig. 1). Different adverse pressure gradients can be tested changing the end-wall opening angle. For the present experiments, the opening angle of the channel (α) has been set to 7, 9 and 12 degrees which correspond to an acceleration parameter $AP = \frac{L}{U_{\infty,0}} \frac{\Delta U_\infty}{\Delta x}$ equal to −0.18, −0.27 and −0.41. Here L is the plate length, $U_{\infty,0}$ is the free-stream velocity at the channel throat and $\frac{\Delta U_\infty}{\Delta x}$ is the velocity gradient along the rear part of the plate.

In order to test the effects of $FSTI$ variation, different turbulence generating grids have been used. Grids are characterized by different mesh sizes and are located 500 mm upstream of the plate leading edge. The lowest $FSTI$ (1.5%) condition is related to the characteristic turbulence of the wind tunnel, since no grids are employed for this case. Table 1 summarizes the turbulence properties and geometrical parameters (rod diameter d, mesh size M and porosity P) of the different grids.

The $FSTI$ level has been computed as the root mean square of the streamwise velocity fluctuations measured by means of Laser Doppler Velocimetry instrumentation. Velocity data has been acquired in the free-stream region, near the plate leading edge, at an average sampling rate of about 10 kHz and for a sampling period of 120 s. It has to be mentioned that the $FSTI$ was varied to match the typical free-stream turbulence intensity found in internal aerodynamic applications. As a result, streaks may develop in the fore part of the separated shear layer

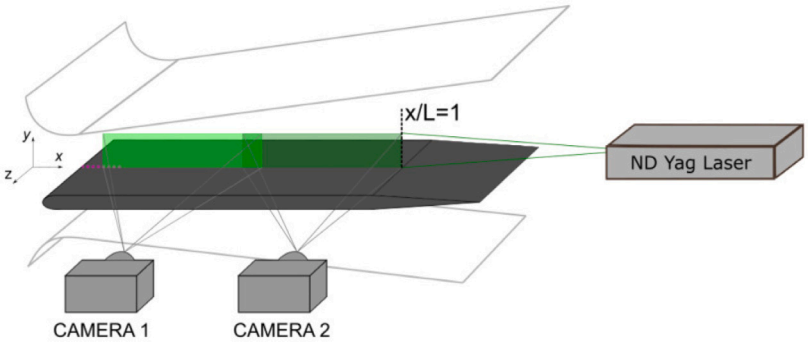

Fig. 1. Test section and PIV instrumentation layout. Green boxes indicate the PIV measuring domain. (For interpretation of the references to color in this figure caption, the reader is referred to the web version of this article.)

(Verdoya et al., 2021). However, it will be shown that the growth of disturbances causing the shear layer transition is still driven by the K-H instability process. For each combination of the $FSTI$ level and APG, eight Reynolds numbers (Re_L) based on the plate length (L) and the leading-edge free-stream velocity $U_{\infty,0}$ have been tested. The overall test matrix therefore accounts for 72 flow cases.

Measurements with particle image velocimetry (PIV) have been performed in a wall-normal plane aligned with the meridional section of the plate (see the green boxes in Fig. 1). In order to reduce the laser reflections, the plate has been black painted. Two cameras with an overlapping field of view have been used simultaneously to capture the boundary layer development from the channel throat to the end of the flat part of the plate. More specifically, the measuring domain extends from $x/L = 0.2$ to $x/L = 1$ in the streamwise direction, and from the wall up to $y/L = 0.04$ in the normal to the wall direction. As it will be discussed in the following, having a fixed extension of the PIV domain for different bubble configurations may lead to marked differences in the snapshot energy when varying the flow parameters. A proper normalization of the data has been therefore applied before computing POD, as discussed in Section 3. The final measuring grid accounts for 614 × 48 measuring points. The spatial resolution and the domain extension here considered allow the characterization of the vortical structures shed for the high Reynolds number cases with around 14 × 9 vectors, while for the lowest Reynolds number condition they increase to 21 × 18. For what concern the domain extension, such large number of points along the streamwise and normal to the wall directions is necessary to properly capture the mean flow deformation of the bubble that basically affect the whole field of view.

The PIV instrumentation is constituted by a dual-cavity ND:YLF pulsed laser Litron LDY 300 (energy 30 mJ per pulse at 1000 Hz repetition rate, 527 nm wavelength) and two SpeedSense M340 digital cameras with a cooled 2560 × 1600 pixels CMOS matrix. The optical system creates a laser sheet of 1 mm thickness which lights seeding vaseline oil particles with a mean diameter of 1.5 μm. In the present experiments, the magnification factor has been set to about 0.16, providing a particle image diameter of about 3 pixels, with a seeding concentration of around 4–5 particles per investigation area. A multi-grid algorithm has been adopted for the computation of the adaptive cross-correlation of PIV images. A final interrogation area of 16 × 16 pixels and 50% overlap has been used. This corresponds to a vector grid spacing of 0.41 mm. A peak validation has been used to discriminate between valid and invalid vectors. Furthermore, a Gaussian fitting procedure has been adopted to guarantee a sub-pixel recognition accuracy of particle displacement equal to 0.1 pixel. Based on the PIV setting, the uncertainty in the instantaneous velocity measurements is estimated to be smaller than 3% in the free-stream regions and approximately equal to 6% in the boundary layer. The uncertainty estimation of the measured velocity field has been carried out considering the peak-ratio method proposed by Charonko and Vlachos (2013). This method is implemented in the commercial software DynamicStudio 7.3, adopted for the current measurements, and correlates the particle displacement uncertainty to the ratio between the dominant correlation peak and the second highest one, see also Wilson and Smith (2013).

For each of the 72 combinations of the flow parameters, 6000 snapshots have been acquired at a sampling rate of 1 kHz. The sampling frequency and overall acquisition period have been set to resolve velocity fluctuations above 1/6 Hz. This allows solving the vortex shedding process in the high Reynolds case with at least 10 snapshots, and the number of snapshots per period increases with reducing Reynolds number. The whole data matrix accounts for 432000 PIV images, that have been used to construct a unique snapshot matrix containing information on the effects due to the flow parameter variation on both the statistical and dynamic response of short and long laminar separation bubbles. It is important to note that the real rank of the dataset snapshot matrix used for the POD analysis described in the following is also influenced by the sampling parameters adopted. The frequency resolution may introduce an "oversampling" factor by an order of 10 for the lowest Reynolds number conditions. Hence, it has been estimated that the real rank of the matrix is about 1 orders of magnitude smaller that the geometrical one (around 1500).

3. Data post processing techniques in high performance computing environment

Thanks to its ability to condense data variance, POD (Lumley, 1970, Berkooz et al., 1993) has been adopted to provide a low-order representation of changes in the time-mean flow structure and vortex shedding characteristics of a LSB. Due to the large data matrix analyzed in this work, the POD algorithm has been implemented in a parallelized version to take advantage of HPC framework, see e.g., Bi and Ono (2013), Akhtar et al. (2010) and Sayadi and Schmid (2016). The present database has been managed in Galileo100, the new High Performance Computer of CINECA. The currently employed decomposition pipeline is schematically summarized in Fig. 2 and it comprises the following listed steps:

(a) PIV snapshots containing streamwise (u) and wall-normal (v) velocity components have been arranged in column vectors sizing $58944 = 614 \times 48 \times 2$.
(b) Sub-matrices (A_i) are formed containing all 6000 snapshots and eight Reynolds numbers for the ith combination of $FSTI$ and APG. Matrices A_1-A_9 have been filled accordingly, with the size of each being 58944 × 48000. Here 58944 is the number of measuring points for the two velocity components, while 48000 is the number of snapshots for fixed $FSTI$ and APG. Eight processor cores have been used in parallel to build the matrices A_1-A_9, while an additional core has been used to generate the whole data matrix A.

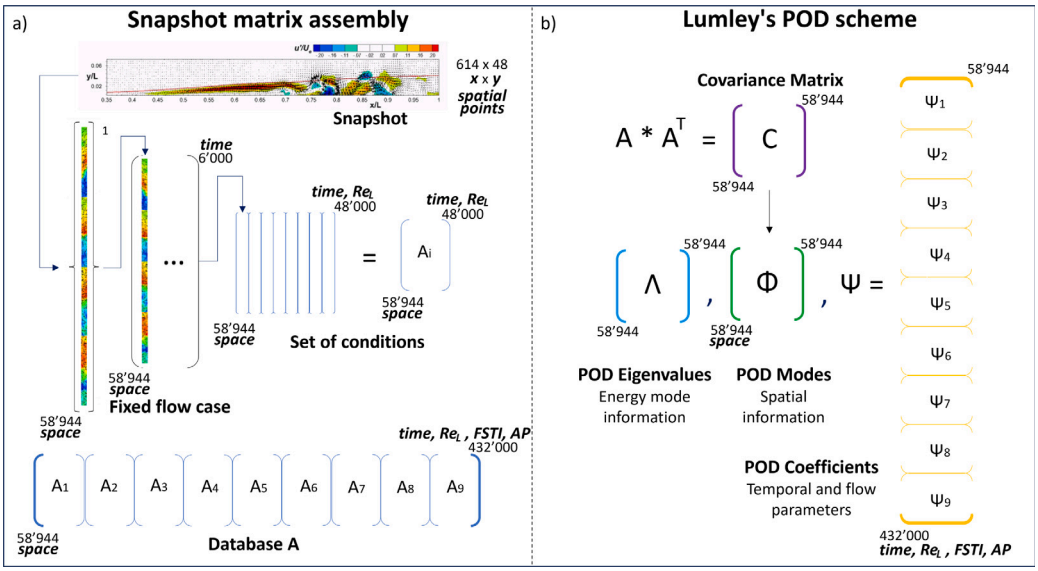

Fig. 2. Schematic visualization of the generation of the PIV snapshot matrix (figure 2.a) and Lumley's POD algorithm (figure 2.b).

(c) Since each snapshot (i.e. each column vector of the A matrix) is characterized by different variance, a suitable normalization has been applied to make all snapshots comparable in terms of their energy content, e.g., (Fogleman et al., 2004; Voisine et al., 2011; Dellacasagrande et al., 2021). This was also necessary to limit the effects of having larger portions of the field of view being characterized by strong fluctuations for the long bubble cases compared to the short ones.

(d) The mean of the entire database (the average of the time-means of each flow condition) has been removed. With such kind of data centering, the first modes will be shown to represent the variation of the time-mean statistical properties characterizing each subset of data with respect to the overall one.

(e) The original Lumley's POD formulation has been applied with the aim of calculating a computationally more convenient covariance matrix $C = AA^T$ of dimensions 58944 × 58944. In HPC environment, the covariance matrix has been computed as the sum of the correlation between each sub-matrix A_i as $C = \sum_{i=1}^{9} A_i A_i^T$. POD modes ($\Phi$) and eigenvalues ($\Lambda$) has been obtained from the eigen-solution of C.

(f) POD coefficients Ψ have been computed by projection as $\Psi = A^T\Phi$. In HPC environment, POD coefficient matrices (Ψ_1 to Ψ_9 in Fig. 2) can be calculated in parallel as the projection of each set of conditions (A_1 to A_9) on the corresponding POD modes, i.e. $\Psi_i = A_i^T\Phi$. Accordingly, POD coefficients can be fragmented in sub-distributions Ψ_i describing the temporal evolution of the corresponding mode for the eight different flow Reynolds number embedded in each sub-matrix A_i. The other partitions of the POD coefficient instead trace the effect due to $FSTI$ and APG variation.

With the aim of providing a rationale for the interpretation of the POD coefficients provided in this work, Fig. 3 shows POD coefficient 1 with its sub-components (Ψ_i) highlighted. It is shown that the coefficients obtained by the present POD algorithm retain both the temporal dynamics of the corresponding modes as well as their changes due to Re_L, $FSTI$ and APG variation. More specifically, the first 6000 elements of the coefficient shown in Fig. 3 provide the mode dynamics at fixed Re_L, $FSTI$ and APG. This and the successive 7 blocks of 6000 elements each describe the effects of changing the Reynolds number, while the additional elements capture all the possible combinations of free-stream turbulence intensity and pressure gradient.

Due to the large size of the mixed POD coefficient matrix, the time-averaged, root mean square values and frequency spectra of the POD coefficients of each case have been computed to further reduce the data. The resulting condensed representations of the mixed coefficients and their leading frequencies will be shown to retain the effects due to the flow parameter variation on the modes and, consequently, on the statistical and dynamic properties of a laminar separation bubble. Modes describing the time-mean response of the separated shear layer and those capturing the modification of the vortex shedding characteristics will be identified based on the frequency spectrum of the corresponding POD coefficients to provide reduced order models of the flow. The peak frequency contained in the vortex shedding mode of the different conditions has also been converted in Strouhal number and then compared with available literature data.

4. Results

4.1. LSB topology and dynamics in the physical space

Fig. 4 reports contour plots of the time-average streamwise velocity fields ($\bar{u}$), scaled by its free-stream value at the measuring domain inlet (U_e). The effect of varying Re_L, $FSTI$ and APG on the time-mean structure of a LSB is shown. The top plots refer to the case at AP=−0.41 and $FSTI$=3.5%. This combination of pressure gradient and free-stream turbulence is taken hereafter as reference. Boundary layer separation was seen to vary from about x/L=0.42 to x/L=0.46 as the Reynolds number increases. Earlier reattachment occurs while switching from the lowest to the highest Reynolds numbers, and the separated flow region shrinks following the expected reduction of the bubble size (Dellacasagrande et al., 2020). It is mentioned here that both short and long bubble states occurred when changing the Reynolds number, as discussed in the previous authors' work (Dellacasagrande et al., 2023, 2024). The first plot shown in Fig. 4 (Re_L=17500, i.d., $U_{\infty,0}$=0.9 m/s) depicts a long laminar separation bubble, whereas short ones are observed at Re_L=29500 (i.d., $U_{\infty,0}$=1.5 m/s), Re_L=38500 (i.d., $U_{\infty,0}$=1.9 m/s) and Re_L=55000 (i.d., $U_{\infty,0}$=2.8 m/s). Then, the bursting process occurs for an intermediate value in the Re_L range 17500–29500.

The center plots of Fig. 4 show LSBs for similar Reynolds numbers but at lower $FSTI$. At lower free-stream turbulence the enlargement of the laminar separation bubble is observed (Istvan et al., 2018). According to previous studies (Simoni et al., 2017), the increase of the size of the LSB is due to the lower disturbance levels within the separated shear layer rather than to modification in the boundary

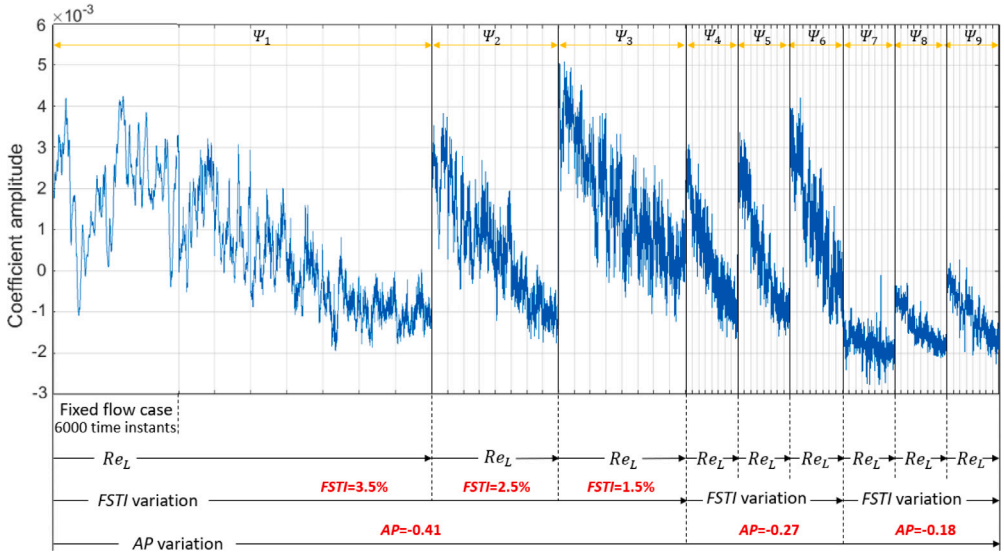

Fig. 3. Schematic visualization of the first POD coefficient and its sub-components.

layer stability characteristics. For the smallest Re_L the bubble becomes remarkably thicker with the shear layer moving far from the plate surface. As further discussed in the following, marked low-frequency shear layer fluctuations have been also observed for this kind of flow conditions (Eljack et al., 2021).

When reducing the adverse pressure gradient (bottom plots, AP=−0.27) the occurrence of thinner but slightly longer bubbles has been detected. This increase in the bubble length is due to the larger BL momentum thickness at the separation position altering the stability characteristics of the separated shear layer (Curle and Skan, 1957). Results shown in Fig. 4 provide an overall view of the statistical response of a LSB to the flow parameter variation that will be captured by the decomposition pipeline described in Section 3.

With the aim of discussing the main structures driving the transition process of the separated shear layer in case of both short and long LSB type, PIV snapshot sequences are shown in Fig. 5 for the lowest and the highest Reynolds numbers at AP=−0.41 and $FSTI$ = 3.5%. As above mentioned, these flow cases refer to a long and a short bubble state, respectively (Dellacasagrande et al., 2023). Contour lines of the time-mean streamwise velocity are also superimposed to the plots to highlight the average structure of the laminar separation bubbles. For the case Re_L = 17500 (top plots), velocity fluctuations are seen to grow in the separated shear layer up to the maximum displacement of the laminar separation bubble. Near this position, large scale vortical structures are formed (see the blue circles in the figure). The first snapshot shows a large scale structure in the region of maximum shear at about x/L=0.82. The intensity of such spanwise vortex is seen to grow at almost fixed position in the following frame and it successively breaks down giving origin to a couple of smaller vortices, which are confined in the dead air region (they occur below the iso-velocity line at $\bar{u}/U_e$=0). Similar observation were made in previous literature works concerning with disturbance growth in short and long laminar separation bubbles, e.g., Sengupta et al. (2019), Rodríguez et al. (2021), Jaroslawski et al. (2023).

A different scenario can be observed at the highest Reynolds number (Re_L=55000 bottom plots of Fig. 5), for which a short LSB has been found to occur. Counter rotating vortices are seen to form near the bubble maximum displacement position as a consequence of the inviscid Kelvin–Helmholtz instability, e.g., Hosseinverdi and Fasel (2019), Toppings and Yarusevych (2022). These vortices evidently grow in the streamwise direction (see the blue arrows in the plots) and then break down into finer scale structures. A convective type instability is expected to characterize the formation and growth of such spanwise structures in the short bubble configuration. Vortices growing in time within the recirculating flow region were not observed for the high Reynolds number cases. The same change in the dynamics leading to the shear layer transition has been observed for the other combinations of APG and $FSTI$ when varying the Reynolds number. Since the currently adopted $FSTI$ levels may lead to the formation of streaks in the separated shear layer (Verdoya et al., 2021), the streamwise distribution of the root mean square of wall-normal fluctuations, whose behavior is affected by the onset of K-H instability (Istvan and Yarusevych, 2018), has been analyzed for the reference conditions. The left plot of Fig. 6 shows that a quasi-exponential trend (see the straight lines in the semi-logarithmic plot), which is typical of Kelvin–Helmholtz like type instability, is observed near the bubble maximum height. The right plot of Fig. 6 shows the frequency spectra of the wall-normal velocity, computed at the position of maximum root-mean-square value for the reference cases. The frequency spectra clearly show bumps, especially in the highest Reynolds number cases, which can be related to the typical vortex shedding frequencies driven by the K-H convective type of instability (Singh, 2019).

4.2. Inspection of dataset energy rank

To investigate the possibility of capturing the response of a LSB to Re_L, $FSTI$ and APG variation within a reduced low-dimensional state-space, the snapshot matrix containing all the acquired data sequences has been post-processed by means of the Proper Orthogonal Decomposition, as mentioned in Section 3. Since POD is an energy-ranked decomposition technique (Berkooz et al., 1993), it is assumed as the most suitable one for the reduction of the present dataset. Fig. 7 depicts the cumulative distribution of the first 1000 POD eigenvalues. It has to be noted that the first 7 leading modes (whose interpretation will be provided in the following) accounts for 80% of the variance of the entire database, while only 200 modes out of the snapshot matrix real rank (hence, about 15% of modes) are needed to reconstruct the original flow field with a truncation error of about 1%. It is mentioned that the truncation error estimated by the cumulative distribution of the POD eigenvalues refers to the overall flow cases, while the error associated with each flow configuration may vary for the different combinations of the flow parameters. This means that the same subset of mode (either 7 or 200 according to the λ distribution) can better reconstruct one particular flow condition with respect to another. In order to better specify the reconstruction error for each flow case, the energy of the original vector field (E) and the energy of the low rank

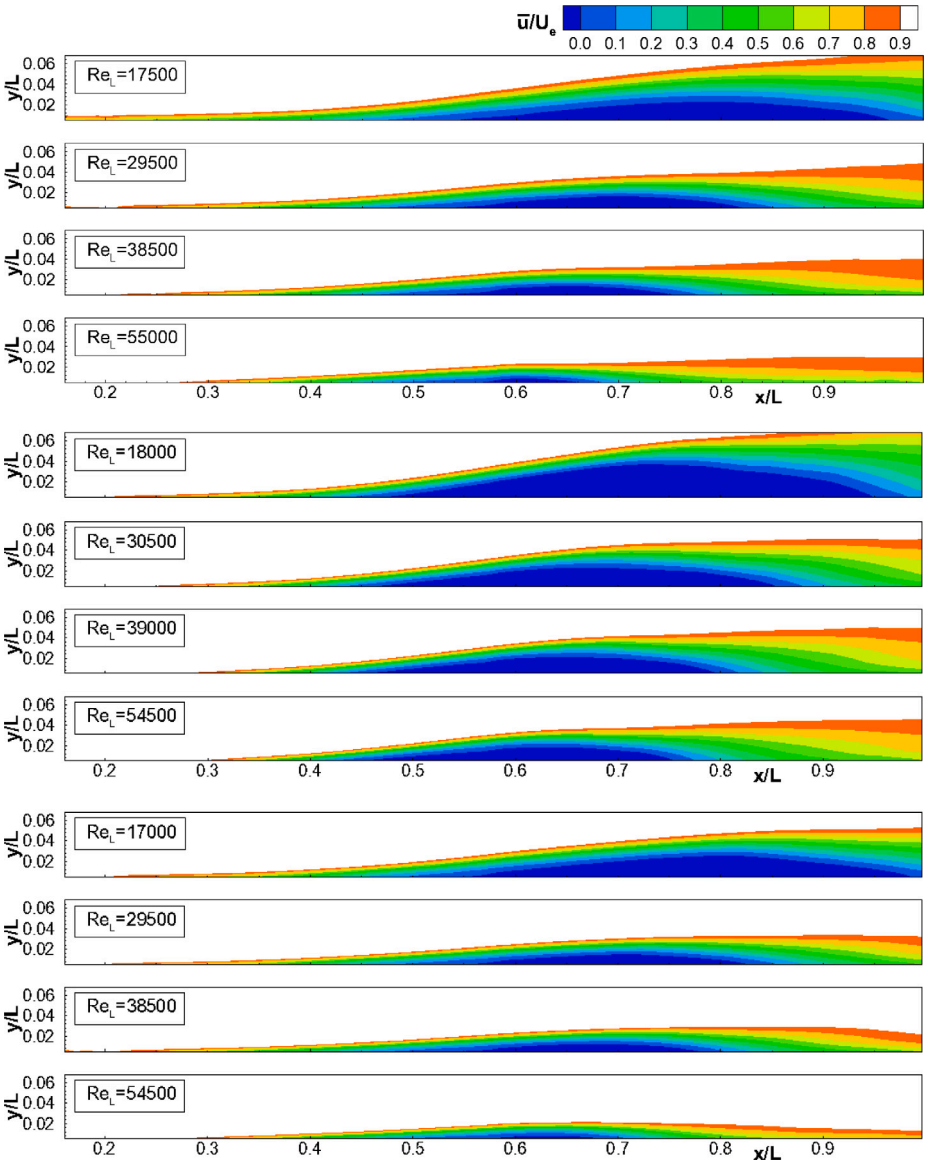

Fig. 4. Contour plots of the normalized time-average streamwise velocity $\bar{u}/U_e$ for variable Reynolds number: (top) $AP = -0.41$ and $FSTI = 3.5\%$, (center) $AP = -0.41$ and $FSTI = 1.5\%$, (bottom) $AP = -0.27$ and $FSTI = 3.5\%$.

Table 2
200 POD modes truncation error for the cases reported in Fig. 4.

$AP = -0.41$ $FSTI = 3.5\%$		$AP = -0.41$ $FSTI = 1.5\%$		$AP = -0.27$ $FSTI = 3.5\%$	
Re_L [ ]	err[%]	Re_L	err[%]	Re_L [ ]	err[%]
17500	0.53	18 000	0.96	17 500	1.22
29500	0.99	30 500	1.45	29 500	1.37
38500	1.56	39 000	1.89	38 500	1.52
55000	2.97	54 500	2.80	55 000	2.14

reconstruction obtained with 200 modes (E_n) have been compared to define the metric error as $err = \frac{\overline{\overline{E}} - \overline{\overline{E_n}}}{\overline{\overline{E}}}$, where $\overline{\overline{*}}$ indicates both temporal and spatial average. Table 2 reports the reconstruction errors of low-rank models based on the first 200 POD modes for the same flow cases shown in Fig. 4.

The truncation error is poorly influenced by the variation of the $FSTI$ and it is slightly more sensitive to changes in the pressure gradient. The error distribution is primarily influenced by the Reynolds number, increasing as the Reynolds number increases. This confirms that the spatial extent is sufficiently large to correctly represent the long bubble cases (low Reynolds number). On the other hand, as the Reynolds number increases, a wider range of scale is expected to occur within the flow and the smallest observable ones will reduce (see e.g., Fig. 4). Accordingly, a larger number of modes is necessary for an accurate reconstruction of the flow field. Similarly, varying Re_L and also APG leads to a marked change in the LSB position and extension, thus requiring an enriched subset of modes for the proper localization of the bubble and the vortex shedding process. Nevertheless, the truncation error remains lower than 3% for the case $AP = -0.41$, $FSTI = 3.5\%$ and $Re_L = 55000$ (highest Re_L and AP). The inherent optimality of the POD procedure together with the currently adopted normalization of the data (see Section 3) allow the considerable reduction of the state space dimensions on which the response of a LSB is seen to evolve.

4.3. POD modes and coefficients

This section discusses the first seven POD modes and coefficients, which have been found to capture the LSB response to the inlet flow parameters. Low-rank representations of the flow field embedding the

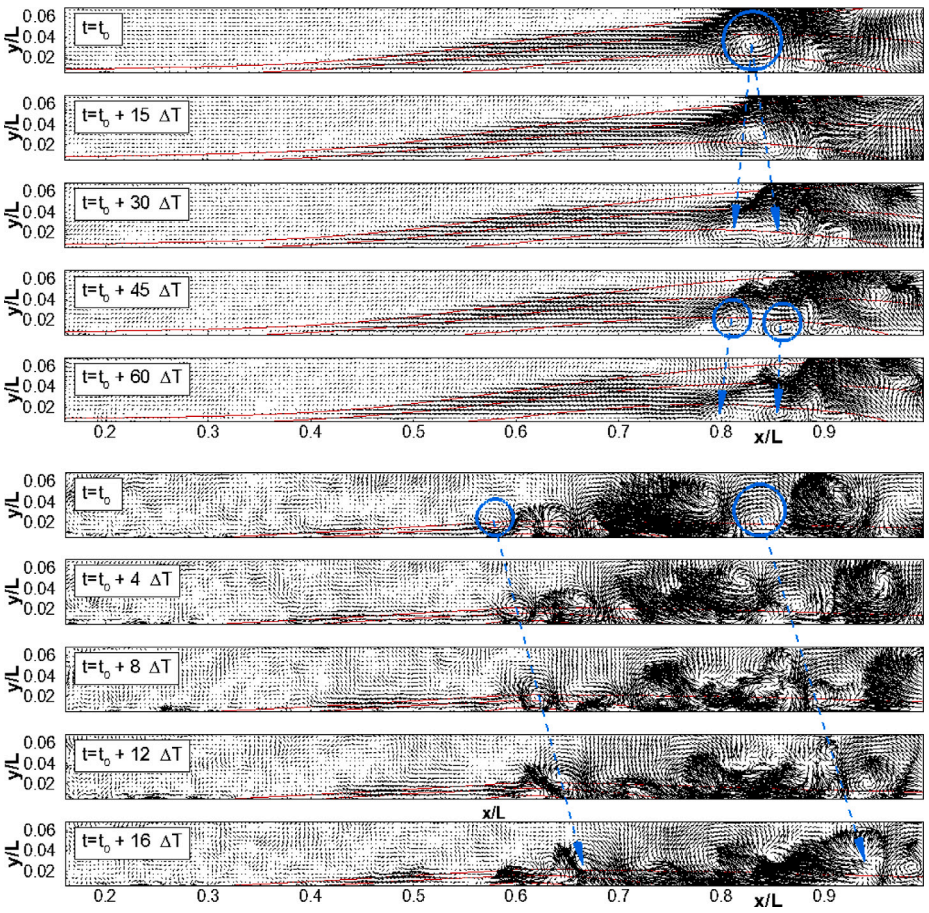

Fig. 5. Vector maps of the instantaneous fluctuating velocity for $AP = -0.41$ and $FSTI$=3.5%: (top) Re_L=17500 and (bottom) Re_L = 55000. Iso-contour lines of $\bar{u}/U_e$=0, 0.5 and 0.9 are shown.

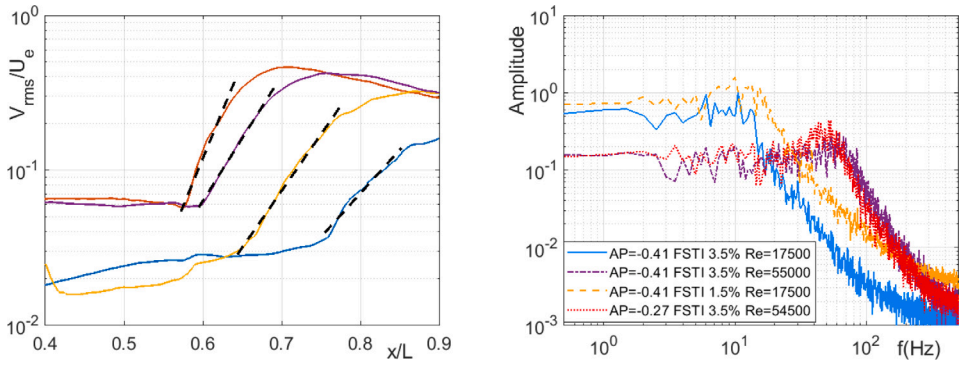

Fig. 6. Streamwise growth of wall-normal fluctuations v_{rms}/U_e (on the left) and frequency spectra of the velocity v-component at the maximum rms position (on the right).

change in the time-mean bubble structure and dynamics have been obtained with this sub-set of modes out of the overall ones. Based on the frequency content of POD coefficients, the first three modes have been recognized as representative of the time-mean response of the bubble and low-frequency shear layer fluctuations, whereas modes from four to seven capture the response of the shedding process to the variation of Re_L, $FSTI$ and APG.

4.3.1. Mean flow response to flow parameters variation and shear layer fluctuations: modes 1–3

Fig. 8 depicts the streamwise component (ϕ_u) of the first three POD modes, while Fig. 9 reports sub-sequences of POD coefficient 1 corresponding to four combinations of Re_L, $FSTI$ and APG. The corresponding frequency spectra are also shown. The second and third POD coefficients retained similar dynamics as for the first one, thus they are not shown here for brevity. Modes 1–3 presented in Fig. 8 show elongated patterns within the separated shear layer. The combination of these modes, once multiplied by the corresponding coefficients, mostly provides the modification of the time-mean structure of the bubble depending on Re_L, $FSTI$ and APG. Limited temporal fluctuations of the sub-components of coefficient 1 are indeed observed in Fig. 9, which were linked to low frequency motions of the bubble. Among the four cases reported here, the low Re_L ones (blue and orange curves) show positive sign of the first coefficient, thus, once combined with mode 1 (first plot of Fig. 8) they provide the enlargement of the recirculating flow region compared to the averaged distribution of the dataset. Contrarily, the reduction of the reversed flow region is provided for the high Re_L cases. The role of mode 1 in the definition

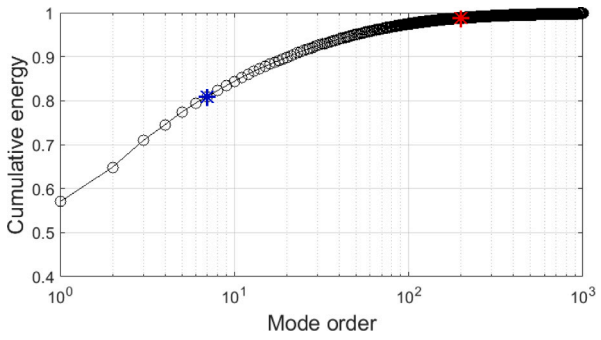

Fig. 7. Normalized cumulative plot of first 1000 POD eigenvalues. Blue and red marks highlight the energy of partial reconstructions based on 7 and 200 modes, respectively. (For interpretation of the references to color in this figure caption, the reader is referred to the web version of this article.)

of the time-mean bubble shape is highlighted also by the frequency spectra reported in Fig. 9 (right plot). The frequency spectrum rapidly drops to zero without showing any deterministic peak typical of the shedding modes, e.g., Simoni et al. (2017). The low-frequency content of the POD coefficients confirms that the modes analyzed here mostly capture the mean flow response as well as low frequency deformation of the LSBs. Low frequency motions become more prominent at low Reynolds number for which higher energy content is observed below 10 Hz. LSBs at low Reynolds number have been found to be more prone to breath and flapping motions than at higher Re_L, showing large scale shear layer fluctuations (see Fig. 5). Modes 2 and 3 have been found to also adjust the bubble shape in streamwise (mode 2) and wall-normal (mode 3) direction. Both these modes show indeed region of opposite sign in the fore and rear parts of the bubble. Low-rank reconstructions of the original database presented in the following will be shown to capture all the aforementioned modification of the LSB due to changes in the external flow parameters.

4.3.2. Dynamic response of a LSB to flow parameters variation: modes 4–7

Fig. 10 shows the contour plots of the streamwise component of modes 4–7. Sub-components of the fourth POD coefficient showing the same cases reported in Fig. 9 are depicted in Fig. 11 together with their corresponding frequency spectra. Coefficients from 5 to 7 have similar dynamical content, thus they are not shown here for brevity. Modes 4–5 and 6–7 present regions of opposite sign of the same size alternating in the streamwise direction, but shifted of 1/4 of the observable wavelength. This is the typical pattern of K-H related modes (Lengani et al., 2014; Dellacasagrande et al., 2020). Modes 4–5 therefore provide the statistical representation of the dominant K-H wavelength among the overall flow cases, whereas modes 6–7 provide its second harmonic. Due to the unsteady nature of K-H related modes, the time-variance of POD coefficient 4 is remarkably increased compared to coefficient 1, capturing the quasi-periodic fluctuations carried by spanwise rollers (the rms of POD coefficients will be reported in Section 4.5). Long LSB (developing at low Re_L) are characterized by the occurrence of large scale vortical structures and shear layer motions, provoking enhanced fluctuations near the reattaching region. Accordingly, the POD coefficient for the low Re_L cases exhibit larger oscillations than at higher Reynolds number, for which short LSBs occur. The Fourier transform of the sub-sequences of the POD coefficient (right plot of Fig. 11) shows high energy in the low frequency range at low Re_L, as in Fig. 8. However, all spectra show localized bumps, which are associated to the quasi-periodic K-H spanwise vortices. The increment of the K-H central frequency with Reynolds number follows the modification of the BL structure at the separation position, see e.g., Simoni et al. (2017) Hosseinverdi and Fasel (2019), Verdoya et al. (2021). Changing the $FSTI$ and the APG has instead smaller effects in this sense (Boutilier and Yarusevych, 2012). For all cases, the characteristic frequencies highlighted by the K-H related coefficients fall within the typical range $0.6 - 0.7U_e/l$, based on the free-stream velocity U_e and mean bubble length l highlighted in the literature (see for instance Kiya and Sasaki (1983) and Cherry et al. (1984)). The corresponding Strouhal number $St_{\theta,s}$, based on the momentum thickness θ_s and the free-stream flow velocity at the separation position U_s ranges from 0.003 to 0.01, and it increases with the flow Reynolds number according to Samson and Sarkar (2016), Ripley and Pauley (1993), Talan and Hourmouziadis (2002), McAuliffe and Yaras (2008), and Singh (2019). The same modification of the shedding process characteristics due to Re_L variation has been observed for all cases embedded within the present database. This further highlights how the statistical and also dynamic response of a LSB to changes in the influencing parameters can be described in a reduced order state space, whose dimensions are much smaller than the size of the original database.

4.4. Low-order reconstructions of the flow field based on mode clustering

This section presents low-order reconstructions of both short and long laminar separation bubbles based on the mode sub-sets described in Section 4.3. The aim is to highlight their capability in capturing the main dynamics embedded within the flow for different bubble states and flow configurations. Fig. 12 compares three snapshots and the related vorticity contours acquired at Re_L = 17500, $FSTI$=3.5% and AP=−0.41 with their low-rank counterparts obtained with mode sub-sets 1–3, 1–7 and 1–200. They are shown in the first, second, third and fourth plot sequences, respectively. Similarly, Fig. 13 shows low rank representations of the flow case at Re_L = 55000, $FSTI$=3.5% and AP=−0.41. The original and reconstructed vorticity contour plots are compared to show the ability of the different reduced order models to reconstruct the vorticity nuclei for different Reynolds number. Moreover, the time-mean structure of the LSB, as provided by each mode subset, is highlighted for both cases by means of iso-contour lines of the streamwise velocity.

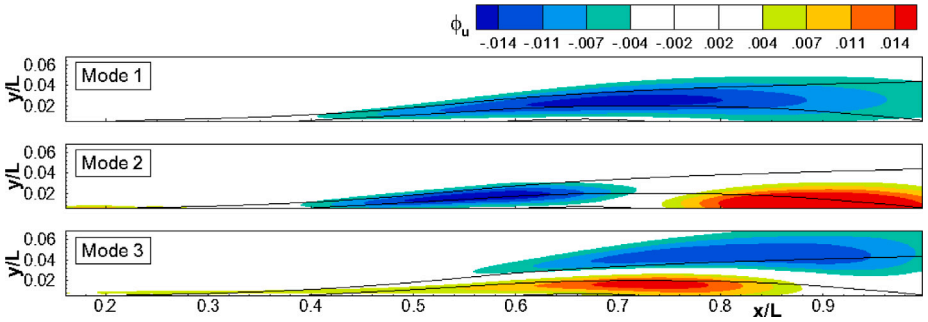

Fig. 8. Contour plots of the streamwise component of the POD modes ϕ_u from 1 to 3. Velocity contour lines of the mean bubble of the entire database equal to $\bar{u}/U_e$=0, 0.5 and 0.9 are over-plotted.

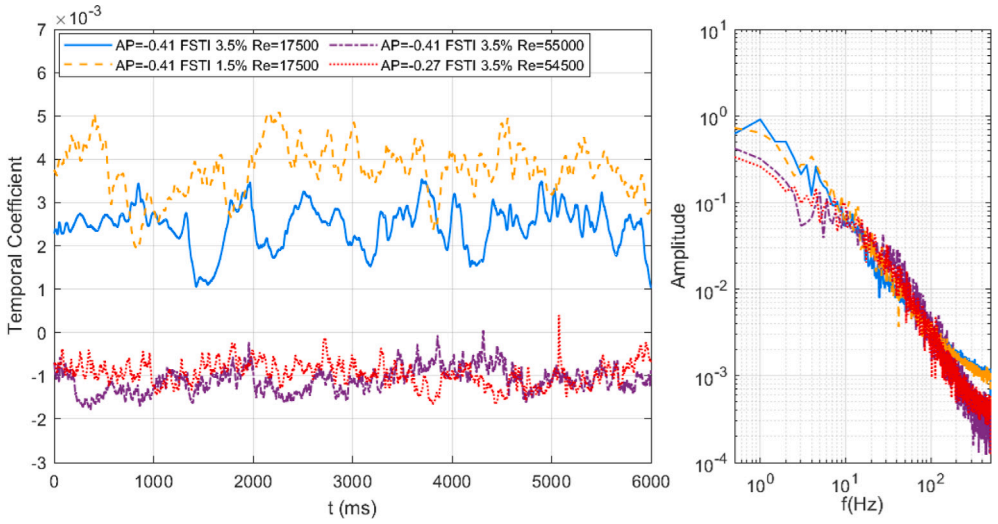

Fig. 9. The time trace (left) and the corresponding frequency spectrum (right) of temporal coefficient of mode 1 for different flow cases.

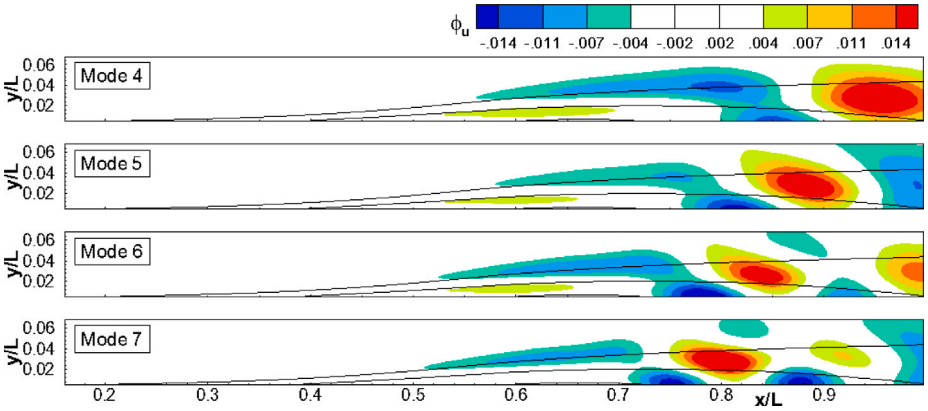

Fig. 10. Contour plots of the streamwise component of the POD modes ϕ_u from 4 to 7. Velocity contour lines of the mean bubble of the entire database equal to $\bar{u}/U_e$=0, 0.5 and 0.9 are over-plotted.

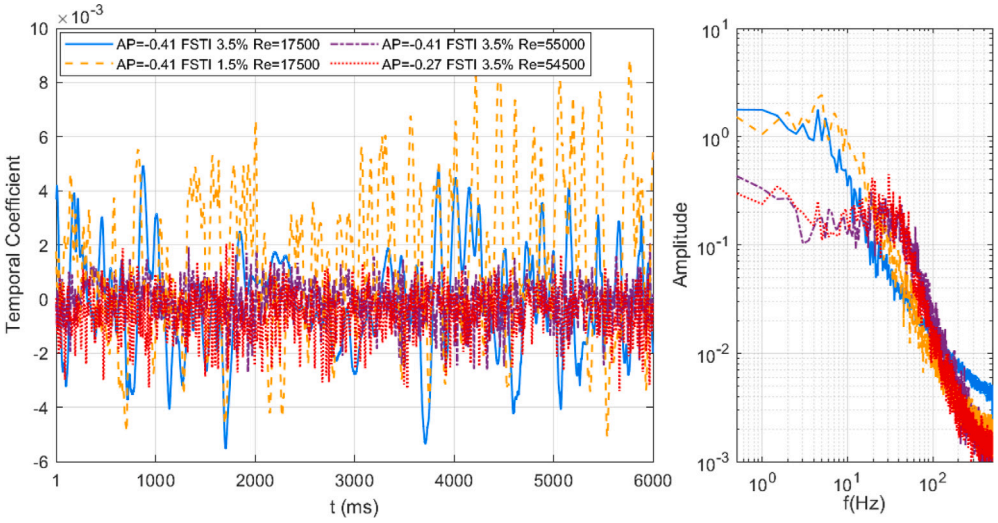

Fig. 11. The time trace (left) and the corresponding frequency spectrum (right) of temporal coefficient of mode 4 for different flow cases.

The second PIV sequence shown in Figs. 12–13 (modes 1–3) highlight the role of the first three POD modes in defining the time-mean structure of a LSB. Indeed, the original and reconstructed iso-contour lines of the u velocity present no appreciable differences. The PIV snapshots show substantially the same spatial distribution over time (the frequency content in these snapshots is almost null). Also, it has to be noted that modes 1–3 already provide the statistical response of the bubble when varying the flow parameters, with the bubble

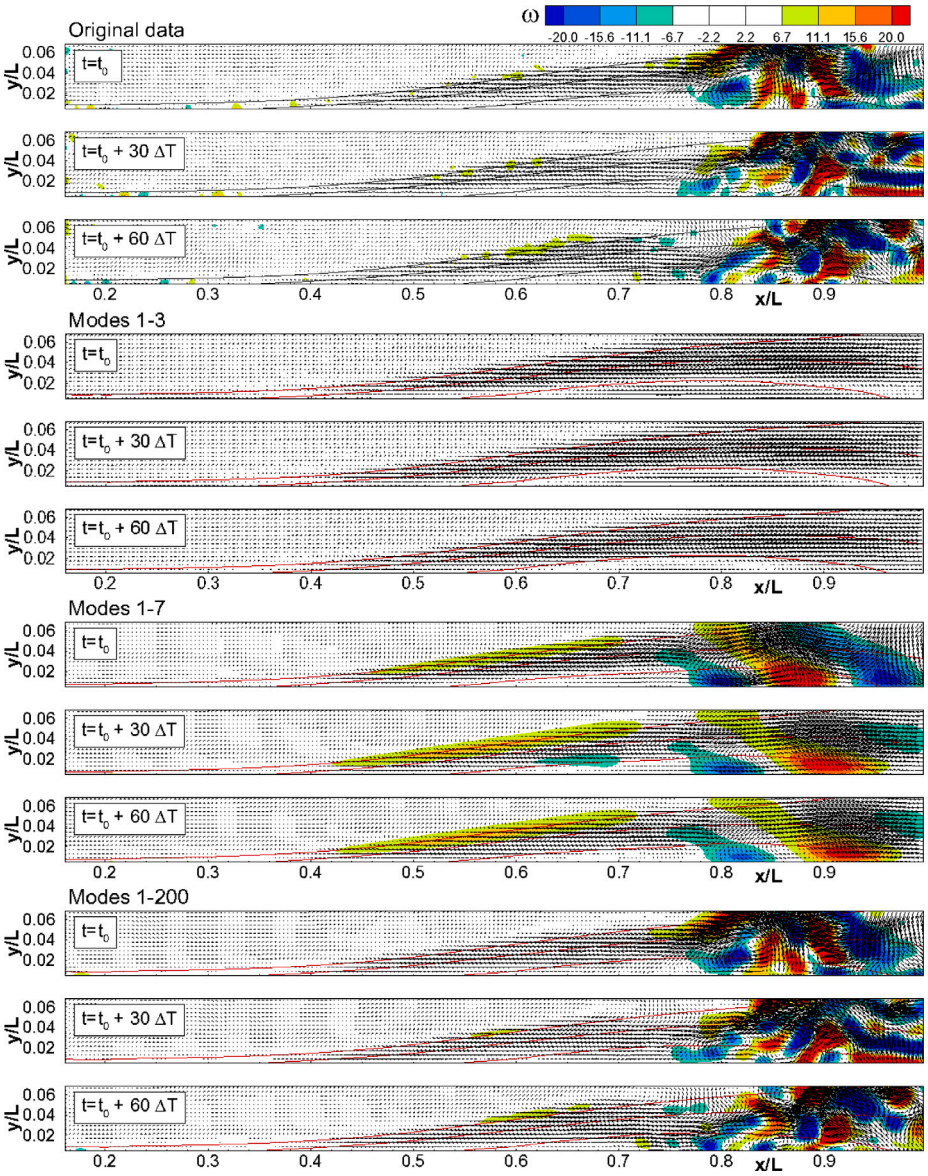

Fig. 12. Comparison of original PIV vector maps and vorticity contours with low-rank reconstructions obtained with modes 1–3, 1–7 and 1–200. The flow case Re_L = 17500, $AP = -0.41$ and $FSTI = 3.5\%$ is reported. Iso-contour lines of time-mean velocity equal to $\bar{u}/U_e$=0, 0.5 and 0.9 are shown.

size significantly reducing between Figs. 12 and 13. Considering the contribution of modes 4–7 to the reconstruction of the flow, it allows capturing the spanwise vortices forming near the bubble maximum displacement position. The adjustment of their scale and location according to the variation of the flow parameter is provided. At low Re_L, a large scale coherent vortical structure with low convective speed is observed. Differently, sequences of counter rotating vortices moving at much higher speed are observed at high Re_L, being indicative of K-H convective rolls, as discussed in Section 4.1. Modes 1–7 are therefore sufficient to capture the notable change in the time-mean and dynamic properties of a laminar separation bubble (LSB) in response to the variation of flow parameters, as confirmed by the analysis of the Strouhal number (St) reported in the previous section. The large-scale vortices captured by these modes accurately represent the position and size of the vorticity nuclei in the long bubble (low Re_L) case. For the high Re_L case, the reconstruction provided by modes 1–7 mainly highlights the same scales and frequencies as the original field, even though vorticity nuclei due to finer scale structures cannot be observed in this low-order reconstruction. Hence, for higher Reynolds numbers, a larger number of modes is required to properly track the vorticity nuclei. As the number of modes is increased (up to 200 modes), finer scale structures are captured by the low-rank representations of the velocity and vorticity fields, as shown in Figs. 12 and 13. This provides a more accurate reproduction of the dominant wavelength embedded in the original vorticity plots, ensuring that even the small-scale vorticity nuclei are properly tracked under both low and high Reynolds number conditions. Hence, they are much closer to the original flow fields, according to the truncation errors reported in Table 2. Data presented here shows that even if 200 modes are required to obtain an highly accurate representation of the flow, the first 7 POD modes alone already allow the description of the modification of the time-mean flow structure, the bubble state, and the largest shear layer dynamics.

4.5. Compressed representation of response of LSBs to flow parameters variation

Data reported in the previous sections has shown the capability of the present data-driven low-order state-space in capturing the time-averaged and dynamic response of a LSB to the variation of the main influencing parameters. With the aim of giving evidence of the low

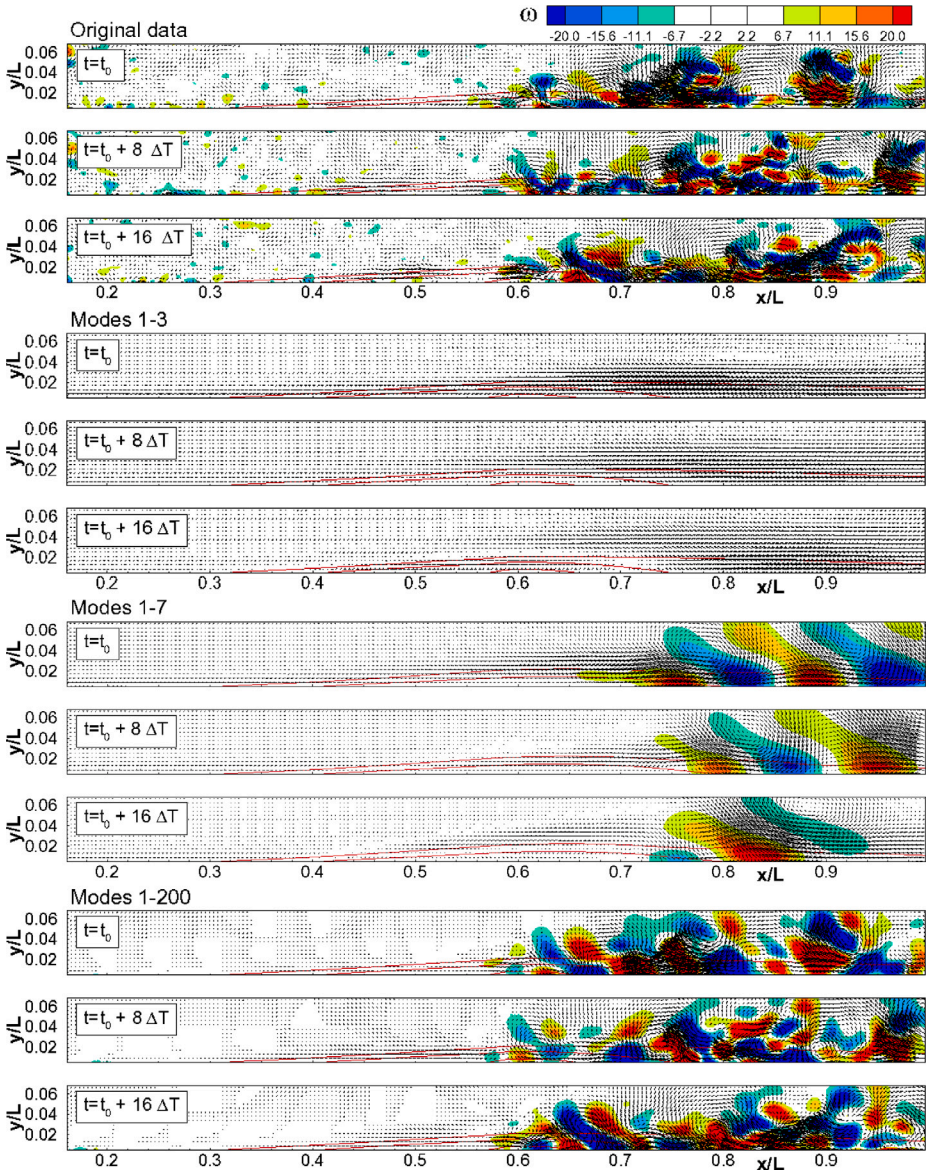

Fig. 13. Comparison of original PIV vector maps and vorticity contours with low-rank reconstructions obtained with modes 1–3, 1–7 and 1–200. The flow case Re_L = 55000, $AP = -0.41$ and $FSTI = 3.5\%$ is reported. Iso-contour lines of time-mean velocity equal to $\bar{u}/U_e$=0, 0.5 and 0.9 are shown.

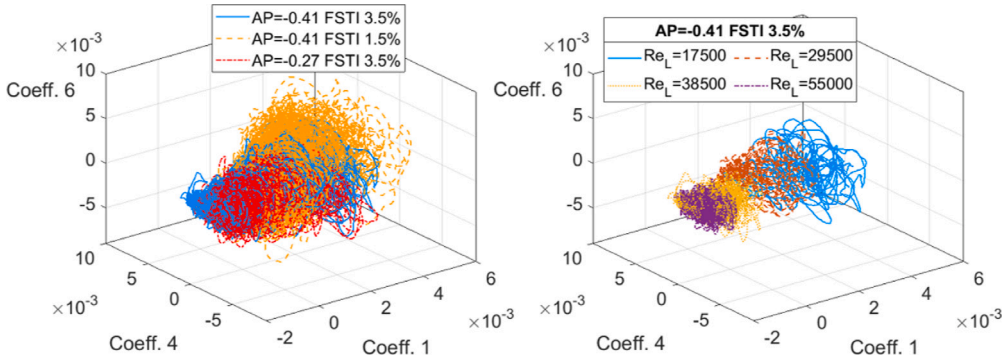

Fig. 14. 3D plot of POD coefficients 1, 4 and 6. The same cases reported in Fig. 4 are shown.

data dispersion in the present POD sub-space, Fig. 14 shows 3D plots of coefficients 1, 4 and 6. The left plot reports three sub-components of the POD coefficients at fixed $FSTI$ and APG for all Reynolds numbers. The right plot highlights the Reynolds number variation in the present POD space for the case $FSTI$=3.5% and AP=−0.41. Based on what has been discussed in Section 4.3, these POD coefficients retain information about changes in the time-mean bubble shape and in central frequency of the vortex shedding process. Each point in the plot is representative

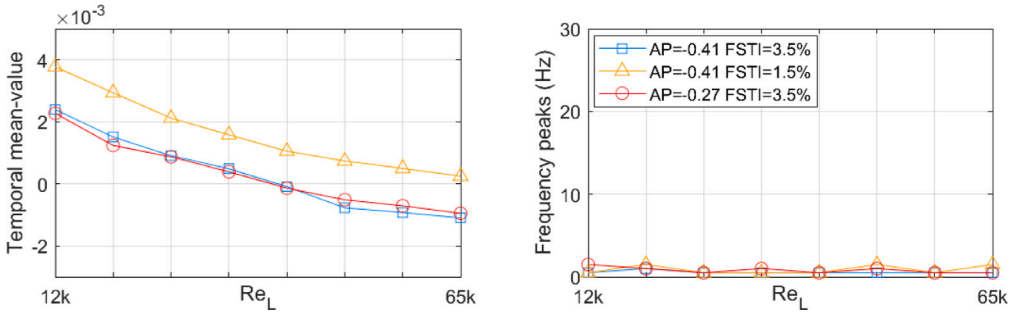

Fig. 15. Condensed representation of POD coefficient 1. The time-mean value and the peak frequency of each flow-case-related time trace are reported in the left and the right plots, respectively.

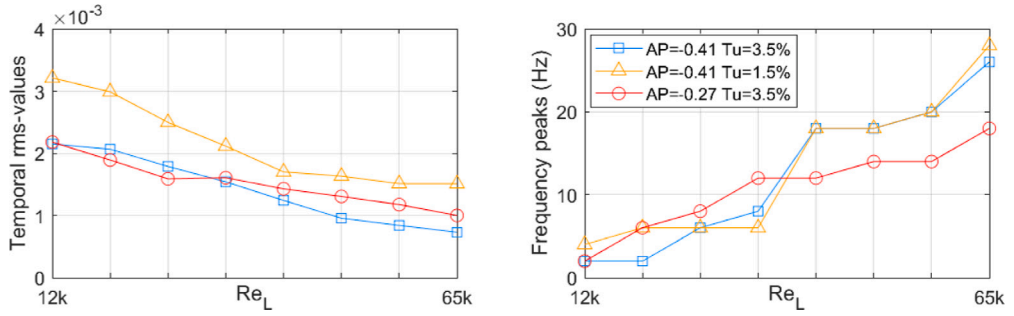

Fig. 16. Condensed representation of POD coefficient 4. The rms value and the peak frequency of each flow-case-related time trace are reported in the left and the right plots, respectively.

of the instantaneous bubble state defined by a set of flow parameters. It has to be noted that the LSBs evolve in a confined region of the present state-space for different combinations of $FSTI$ and APG when varying the Reynolds number. The present results confirm the low dimensionality of the statistical and dynamic response of both short and long bubbles. Accordingly, separated flows evolving under different flow conditions appear to share similarities in the modification of the shape and position of the recirculating flow region as well as in the modification of the shedding process.

Due to the large dimension of the POD coefficients, that depend on both time and flow parameters, their compressed representation in terms of conditional mean value and rms are provided for different values of Re_L, $FSTI$ and APG (the same flow cases reported in Fig. 4 are discussed). The time-mean values of coefficient 1 computed independently for each sub-sequence referring to a specific flow configuration are reported in Fig. 15 together with the associated peak frequency value. This latter is close to zero since these modes retain the deformation of the time-mean bubble shape, as previously discussed. Data are shown against Re_L for different values of inlet turbulence and pressure gradient. The distribution of the conditional mean values provide evidence of the capability of the present reduced POD space in capturing the expected response of a LSB in a statistical sense. The average bubble size reduces indeed when increasing the Reynolds number as well as the free-stream turbulence (Boutilier and Yarusevych, 2012; Toppings and Yarusevych, 2022). The adverse pressure gradient is seen to have lower effects in this sense. However, modes 1 to 3 should be considered to capture the overall time-mean response of the bubble to the flow parameters variation.

Fig. 16 shows the rms of sub-sequences of POD coefficient 4 for the same cases discussed in Fig. 15. The rms is shown here instead of the mean value to better characterize the unsteadiness of K-H related modes. The energy of fluctuations captured by mode 4 is highly sensitive to the Reynolds number. This latter has been shown to be the parameter having the major role in defining the bubble state and the modification of the dynamic properties of a LSB (Dellacasagrande et al., 2023; Toppings and Yarusevych, 2023). The central frequency of the spanwise vortices shed by the laminar separation bubble, as provided by coefficient 4, also strongly depends on this parameter, i.e. the higher Re_L the higher the frequency peak (Boutilier and Yarusevych, 2012). Coefficient 5 has been found to still capture the response of the first harmonic of dominant spanwise rolls to changes in the flow characteristics, while coefficients 6–7 retained the second order one, with this latter showing the same trends as those highlighted here. This compressed representations of the mixed POD coefficients summarize the behavior of the two set of modes here considered, which act properly scaling the time-mean structure of the bubble and the intensity and dynamic content of the dominant shedding vortices. In this sense, an even more sparse representation of the time-mean response of the bubble can be obtained from the present database combining the mean value of coefficient 1 for each flow case with its corresponding mode. Similarly, the rms and peak frequency of different segments of coefficient 4 already provide the underlying periodic fluctuation that better approximate the central frequency of the spanwise shedding rolls. The present results shows that a low-dimensional response of a LSB there exist regardless of the wide range of flow parameters here considered.

5. Conclusions

The present research work discusses the response of a flat plate laminar separation bubble to the variation of the flow Reynolds number, free-stream turbulence intensity and pressure gradient reproducing the typical conditions encountered in internal aerodynamic applications, characterized by quite high $FSTI$ level. Depending on the combination of the flow parameters, short and long laminar separation bubbles have been observed.

The computation of a parallelized version of the POD algorithm in HPC environment has allowed us to inspect similarities in the behavior of a separation bubble evolving under widely different flow conditions. POD modes have been computed from a unique snapshot matrix embedding all the 432000 flow records, even thought the real rank of the snapshot matrix could be an order of magnitude smaller. The POD coefficients therefore incorporates the time variance of the

bubble state as well as its dependence on the Reynolds number, the free-stream turbulence and the pressure gradient. This novel approach allowed us to inspect the existence of a proper state-space capturing the general response of a laminar separation bubble in terms of both statistics and dynamics.

The first 3 leading modes retained the time-mean response of the separated shear layer due to the variation of the influencing parameters. Instead, modes 4–7 captured the statistical response of the dominant shedding frequency and its second harmonic. The Strouhal number computed by the peak frequency provided by the Fourier transform of the leading shedding mode well relies within the range typically observed in the literature. For the low Reynolds number case, these seven modes offer a good reconstruction of the vorticity nuclei induced by the largest scale structures. However, for higher Reynolds numbers, a larger number of modes is required to accurately track the vorticity nuclei. Specifically, 200 modes are necessary to properly reconstruct the dominant wavelength embedded in the original vorticity plots. Under these conditions, both small- and large-scale vorticity nuclei are well represented across low and high Reynolds number cases. POD coefficients provide indeed the time- and flow-case-dependent weights for the corresponding modes to adjust the bubble state and dynamics. In conclusion, the present work points out the existence of a low-dimensional response (both statistical and dynamic) of a laminar separation bubble to the variation of the most influencing parameters.

CRediT authorship contribution statement

Virginia Bologna: Writing – original draft, Formal analysis, Data curation. **Matteo Dellacasagrande:** Writing – review & editing, Data curation, Conceptualization. **Davide Lengani:** Writing – review & editing, Conceptualization. **Daniele Simoni:** Writing – review & editing.

Declaration of competing interest

The authors declare that they have no known competing financial interests or personal relationships that could have appeared to influence the work reported in this paper.

Data availability

Data will be made available on request.

References

Akhtar, I., Borggaard, J., Iliescu, T., Wang, Z., 2010. Closure for improved reduced-order models using high performance computing. In: 48th AIAA Aerospace Sciences Meeting Including the New Horizons Forum and Aerospace Exposition. p. 1276.

Alam, M., Sandham, N., 2000. Direct numerical simulation of 'short' laminar separation bubbles with turbulent reattachment. J. Fluid Mech. 410, 1–28.

Alferez, N., Mary, I., Lamballais, E., 2013. Study of stall development around an airfoil by means of high fidelity large eddy simulation. Flow Turbul. Combust. 91 (3), 623–641.

Aniffa, S.M., Caesar, V., Dabaria, V., Mandal, A., 2023. Characteristics of geometry-and pressure-induced laminar separation bubbles at an enhanced level of free-stream turbulence. J. Fluid Mech. 957, A19.

Avdis, A., Lardeau, S., Leschziner, M., 2009. Large eddy simulation of separated flow over a two-dimensional hump with and without control by means of a synthetic slot-jet. Flow Turbul. Combust. 83, 343–370.

Berkooz, G., Holmes, P., Lumley, J.L., 1993. The proper orthogonal decomposition in the analysis of turbulent flows. Annu. Rev. Fluid Mech. 25 (1), 539–575.

Bi, C., Ono, K., 2013. POD-based parallel compression for visualizing large-scale dataset. In: Proceedings of High Performance Computing Symposium. p. 83.

Boutilier, M.S., Yarusevych, S., 2012. Parametric study of separation and transition characteristics over an airfoil at low Reynolds numbers. Exp. Fluids 52 (6), 1491–1506.

Brinkerhoff, J.R., Yaras, M.I., 2011. Interaction of viscous and inviscid instability modes in separation–bubble transition. Phys. Fluids 23 (12).

Charonko, J.J., Vlachos, P.P., 2013. Estimation of uncertainty bounds for individual particle image velocimetry measurements from cross-correlation peak ratio. Meas. Sci. Technol. 24 (6), 065301.

Cherry, N., Hillier, R., Latour, M., 1984. Unsteady measurements in a separated and reattaching flow. J. Fluid Mech. 144, 13–46.

Curle, N., Skan, S., 1957. Approximate methods for predicting separation properties of laminar boundary layers. Aeronaut. Q. 8 (3), 257–268.

Dellacasagrande, M., Barsi, D., Bagnerini, P., Lengani, D., Simoni, D., 2021. Identification of coexisting dynamics in boundary layer flows through proper orthogonal decomposition with weighting matrices. Meccanica 56 (9), 2197–2217.

Dellacasagrande, M., Barsi, D., Lengani, D., Simoni, D., 2024. Instability processes in short and long laminar separation bubbles. Exp. Fluids 65 (7), 109.

Dellacasagrande, M., Barsi, D., Lengani, D., Simoni, D., Verdoya, J., 2020. Response of a flat plate laminar separation bubble to Reynolds number, free-stream turbulence and adverse pressure gradient variation. Exp. Fluids 61 (6).

Dellacasagrande, M., Lengani, D., Simoni, D., Yarusevych, S., 2023. A data-driven analysis of short and long laminar separation bubbles. J. Fluid Mech. 976, R3.

Diwan, S.S., Chetan, S., Ramesh, O., 2006. On the bursting criterion for laminar separation bubbles. In: IUTAM Symposium on Laminar-Turbulent Transition. Springer, pp. 401–407.

Diwan, S.S., Ramesh, O.N., 2009. On the origin of the inflectional instability of a laminar separation bubble. J. Fluid Mech. 629, 263–298.

Eljack, E., Soria, J., Elawad, Y., Ohtake, T., 2021. Simulation and characterization of the laminar separation bubble over a NACA-0012 airfoil as a function of angle of attack. Phys. Rev. Fluids 6 (3), 034701.

Fogleman, M., Lumley, J., Rempfer, D., Haworth, D., 2004. Application of the proper orthogonal decomposition to datasets of internal combustion engine flows. J. Turbul. 5 (1), 023.

Gaster, M., 1967. The structure and behaviour of laminar separation bubbles. Technical report, Aeronautical Research Council.

Horton, H., 1967. A semi-empirical theory for the growth and bursting of laminar separation bubbles.

Horton, H.P., 1968. Laminar Separation Bubbles in Two and Three Dimensional Incompressible Flow (Ph.D. thesis). Queen Mary University of London.

Hosseinverdi, S., Fasel, H.F., 2019. Numerical investigation of laminar–turbulent transition in laminar separation bubbles: the effect of free-stream turbulence. J. Fluid Mech. 858, 714–759.

Istvan, M.S., Kurelek, J.W., Yarusevych, S., 2018. Turbulence intensity effects on laminar separation bubbles formed over an airfoil. AIAA J. 56 (4), 1335–1347.

Istvan, M.S., Yarusevych, S., 2018. Effects of free-stream turbulence intensity on transition in a laminar separation bubble formed over an airfoil. Exp. Fluids 59 (3), 52.

Jaroslawski, T., Forte, M., Vermeersch, O., Moschetta, J.-M., Gowree, E.R., 2023. Disturbance growth in a laminar separation bubble subjected to free-stream turbulence. J. Fluid Mech. 956, A33.

Jones, L., Sandberg, R., Sandham, N., 2008. Direct numerical simulations of forced and unforced separation bubbles on an airfoil at incidence. J. Fluid Mech. 602, 175–207.

Kiya, M., Sasaki, K., 1983. Structure of a turbulent separation bubble. J. Fluid Mech. 137, 83–113.

Kumar, R., Sarkar, S., 2023. Features of laminar separation bubble subjected to varying adverse pressure gradients. Phys. Fluids 35 (12).

Kurelek, J.W., Tuna, B.A., Yarusevych, S., Kotsonis, M., 2021. Three-dimensional development of coherent structures in a two-dimensional laminar separation bubble. AIAA J. 59 (2), 493–505.

Lengani, D., Simoni, D., Ubaldi, M., Zunino, P., 2014. POD analysis of the unsteady behavior of a laminar separation bubble. Exp. Therm. Fluid Sci. 58, 70–79.

Lumley, J.L., 1970. Stochastic tools in turbulence. Appl. Math. Mech. 12.

Marxen, O., Henningson, D.S., 2011. The effect of small-amplitude convective disturbances on the size and bursting of a laminar separation bubble. J. Fluid Mech. 671, 1–33.

Marxen, O., Lang, M., Rist, U., 2013. Vortex formation and vortex breakup in a laminar separation bubble. J. Fluid Mech. 728, 58–90.

Marxen, O., Lang, M., Rist, U., Wagner, S., 2003. A combined experimental/numerical study of unsteady phenomena in a laminar separation bubble. Flow Turbul. Combust. 71, 133–146.

Marxen, O., Rist, U., Wagner, S., 2004. Effect of spanwise-modulated disturbances on transition in a separated boundary layer. AIAA J. 42 (5), 937–944.

McAuliffe, B.R., Yaras, M.I., 2008. Numerical study of instability mechanisms leading to transition in separation bubbles.

McAuliffe, B.R., Yaras, M.I., 2010. Transition mechanisms in separation bubbles under low- and elevated-freestream turbulence. J Turbomach. 132, 011004–011010.

Mitra, A., Ramesh, O., 2019. New correlation for the prediction of bursting of a laminar separation bubble. AIAA J. 57 (4), 1400–1408.

Nakamura, Y., Ohya, Y., Tsuruta, H., 1991. Experiments on vortex shedding from flat plates with square leading and trailing edges. J. Fluid Mech. 222, 437–447.

Radespiel, R., Windte, J., Scholz, U., 2007. Numerical and experimental flow analysis of moving airfoils with laminar separation bubbles. AIAA J. 45 (6), 1346–1356.

Ripley, M.D., Pauley, L.L., 1993. The unsteady structure of two-dimensional steady laminar separation. Phys. Fluids A: Fluid Dyn. 5 (12), 3099–3106.

Roberts, W., 1975. The effect of Reynolds number and laminar separation on axial cascade performance.

Rodríguez, D., Gennaro, E.M., Souza, L.F., 2021. Self-excited primary and secondary instability of laminar separation bubbles. J. Fluid Mech. 906.
Samson, A., Sarkar, S., 2016. An experimental investigation of a laminar separation bubble on the leading-edge of a modelled aerofoil for different Reynolds numbers. Proc. Inst. Mech. Eng. Part C: J. Mech. Eng. Sci. 230 (13), 2208–2224.
Sandham, N., 2008. Transitional separation bubbles and unsteady aspects of aerofoil stall. Aeronaut. J. 112 (1133), 395–404.
Sayadi, T., Schmid, P.J., 2016. Parallel data-driven decomposition algorithm for large-scale datasets: with application to transitional boundary layers. Theor. Comput. Fluid Dyn. 30, 415–428.
Sengupta, T.K., Sharma, P.K., Sengupta, A., Suman, V.K., 2019. Tracking disturbances in transitional and turbulent flows: Coherent structures. Phys. Fluids 31 (12), 124106.
Serna, J., Lázaro, B., 2015. On the bursting condition for transitional separation bubbles. Aerosp. Sci. Technol. 44, 43–50.
Simoni, D., Lengani, D., Ubaldi, M., Zunino, P., Dellacasagrande, M., 2017. Inspection of the dynamic properties of laminar separation bubbles: free-stream turbulence intensity effects for different Reynolds numbers. Exp. Fluids 58 (6), 66.
Singh, N., 2019. Instability and transition in a laminar separation bubble. J. Appl. Fluid Mech. 12 (5), 1511–1525.
Talan, M., Hourmouziadis, J., 2002. Characteristic regimes of transitional separation bubbles in unsteady flow. Flow Turbul. Combust. 69 (3–4), 207–227.
Tani, I., 1964. Low-speed flows involving bubble separations. Prog. Aerosp. Sci. 5, 70–103.
Toppings, C.E., Yarusevych, S., 2022. Structure and dynamics of a laminar separation bubble near a wing root: towards reconstructing the complete LSB topology on a finite wing. J. Fluid Mech. 944, A14.
Toppings, C., Yarusevych, S., 2023. Transient dynamics of laminar separation bubble formation and bursting. Exp. Fluids 64 (3), 57.
Toppings, C.E., Yarusevych, S., 2024. Laminar separation bubble formation and bursting on a finite wing. J. Fluid Mech. 986, A26.
Tucker, P., 2013. Trends in turbomachinery turbulence treatments. Prog. Aerosp. Sci. 63, 1–32.
Verdoya, J., Dellacasagrande, M., Lengani, D., Simoni, D., Ubaldi, M., 2021. Inspection of structures interaction in laminar separation bubbles with extended proper orthogonal decomposition applied to multi-plane particle image velocimetry data. Phys. Fluids 33 (4), 043607.
Vitkovicova, R., Yokoi, Y., Hyhlik, T., 2020. Identification of structures and mechanisms in a flow field by POD analysis for input data obtained from visualization and PIV. Exp. Fluids 61, 1–21.
Voisine, M., Thomas, L., Borée, J., Rey, P., 2011. Spatio-temporal structure and cycle to cycle variations of an in-cylinder tumbling flow. Exp. Fluids 50 (5), 1393–1407.
Wilson, B.M., Smith, B.L., 2013. Uncertainty on PIV mean and fluctuating velocity due to bias and random errors. Meas. Sci. Technol. 24 (3), 035302.
Wu, W., Meneveau, C., Mittal, R., 2020. Spatio-temporal dynamics of turbulent separation bubbles. J. Fluid Mech. 883, A45.